Available online at www.sciencedirect.com

ScienceDirect

Advances in Space Research 61 (2018) 1636–1651

ADVANCES IN SPACE RESEARCH (a COSPAR publication)

www.elsevier.com/locate/asr

All-sky-imaging capabilities for ionospheric space weather research using geomagnetic conjugate point observing sites

C. Martinis *, J. Baumgardner, J. Wroten, M. Mendillo

Center for Space Physics, Boston University, 725 Commonwealth Ave, Boston, MA 02215, USA

Received 31 March 2017; received in revised form 10 July 2017; accepted 12 July 2017
Available online 2 August 2017

Abstract

Optical signatures of ionospheric disturbances exist at all latitudes on Earth—the most well known case being visible aurora at high latitudes. Sub-visual emissions occur equatorward of the auroral zones that also indicate periods and locations of severe Space Weather effects. These fall into three magnetic latitude domains in each hemisphere: (1) sub-auroral latitudes ~40–60°, (2) mid-latitudes (20–40°) and (3) equatorial-to-low latitudes (0–20°).

Boston University has established a network of all-sky-imagers (ASIs) with sites at opposite ends of the same geomagnetic field lines in each hemisphere—called *geomagnetic conjugate points*. Our ASIs are autonomous instruments that operate in mini-observatories situated at four conjugate pairs in North and South America, plus one pair linking Europe and South Africa. In this paper, we describe instrument design, data-taking protocols, data transfer and archiving issues, image processing, science objectives and early results for each latitude domain. This unique capability addresses how a single source of disturbance is transformed into similar or different effects based on the unique "receptor" conditions (seasonal effects) found in each hemisphere. Applying optical conjugate point observations to Space Weather problems offers a new diagnostic approach for understanding the global system response functions operating in the Earth's upper atmosphere.

Keywords: All-sky imager; Airglow; Ionospheric perturbations; Magnetic field; Conjugate behavior

1. Introduction

1.1. Overview

An all-sky camera is the term used for a scientific imaging system that employs a fisheye lens to record the scene from horizon-to-horizon at all azimuths. It was developed for use at high latitudes in Europe and North America to record the appearance of visible aurora. A summary of the history and use of all-sky auroral imaging systems can be found in the classic books by Eather (1980) and Akasofu (2003).

The Earth's upper atmosphere ($h > 80$ km) also has emission features within the vast regions equatorward of the visible aurora. While auroral emission patterns appear at middle latitudes during severe geomagnetic storms, they are still auroral processes. In this paper we review the methods of observing and analyzing the low-light-level emissions found at latitudes equatorward of the visible aurora. Such emission patterns are related to the morphology of the Earth's magnetic field (**B**), but at latitudes low enough that the geometry of magnetic field lines are not significantly affected by geomagnetic storms. This magnetic domain from the equator to sub-auroral latitudes encompasses **B**-lines that extend to less than ~4 earth radii ($L < 4$).

We have recently established a network of five paired observing sites at both ends of geomagnetic field lines in three latitude domains in each hemisphere: one pair at

* Corresponding author.
E-mail address: martinis@bu.edu (C. Martinis).

http://dx.doi.org/10.1016/j.asr.2017.07.021
0273-1177/

low latitudes, two pairs at middle latitudes, and two pairs at sub-auroral latitudes. This set of *geomagnetic conjugate point* observatories from L ~ 1 to L ~ 3 provides a new capability for studies of ionospheric disturbances ordered by the geomagnetic field. Under such conditions, a fixed disturbance source encounters different seasonal conditions in each hemisphere. *Conjugate point optical aeronomy* thus offers the opportunity to explore single-source/dual-receptor conditions in ways not previously available to the extent now possible. The disturbances to be discussed in the context of conjugate science are equatorial spread F (ESF) (at low latitudes), medium scale travelling ionospheric disturbances (MSTIDs) (at mid-latitudes), and stable auroral red (SAR) arcs (at sub-auroral latitudes).

We are not the first group to pursue conjugate point optical science. There is a rich history of conjugate studies of the visible aurora at high latitudes. For example, see Frey et al. (1999) for discussion of coordinated space-based/ground-based auroral science. At lower latitudes, conjugate point studies of ionospheric storms appear in Kalita et al. (2016). Studies of SAR arcs from conjugate locations are very few. Reed and Blamont (1974) may have been the first to report on conjugate SAR arcs. They described the brightness values and locations of a SAR arc observed in September 1967 via a combination of ground-based observations in the northern hemisphere and satellite data for the southern hemisphere. Pavlov (1997) used observations made by the OV1-10 satellite during a magnetic storm in February 1967 to compare brightness values in both hemispheres (separated in time by ~25 min) and to probe via modeling the roles of key parameters central to the emission process. Our all-sky-imaging observations of SAR arcs from Millstone Hill (MA) and Rothera (Antarctica) to be described below appear to be the first case of simultaneous ground-based optical data sets from both hemispheres.

Simultaneous conjugate optical observations of MSTIDs were carried out for the first time by Otsuka et al. (2004) who showed MSTIDs during the night of 9 August, 2005 in Japan and Australia. Shiokawa et al. (2005) was able to measure conjugate MSTIDs on several nights during a campaign in May-June 2003 that used all-sky imagers in the Japanese/Australian longitude sector. The mapping of electric fields from one hemisphere to the other was assumed to be the main mechanism to explain the observations. Martinis et al. (2011) presented the first observations of simultaneous measurements of MSTIDs in the American sector using all-sky imaging and GPS data. Their results showing high activity during local winter provided support for the importance of local E and F region coupling, in addition to the inter-hemispheric coupling. A recent study by Burke et al. (2016), using data from C/NOFS satellite and all-sky imagers at El Leoncito and Arecibo, showed that 'electric field mapping' occurs by the propagation of Alfven waves generated in the local summer hemisphere.

An early conjugate point study of ESF detected by optical and radio methods was conducted in the Ascension Island longitude sector by combining ground-based and airborne methods (Weber et al., 1983). Their results demonstrated the magnetic field flux-tube coherence of ESF signatures spanning ~3000 km of trans-equatorial distances. Two decades later, much larger-scale studies of ESF onset and evolution using clusters of optical and radio diagnostic instruments were achieved during the Conjugate Point Equatorial Experiments (COPEX) conducted in Brazil in 2002. The all-sky imaging observations from Boa Vista and Campo Grande showed the differences between airglow depletion signatures of large-scale coherence versus small-scale differences, while ionosonde ESF data appeared similar at both sites (Abdu et al., 2009). Sobral et al. (2009) used those optical and radio observations to study plasma dynamics during the same campaign. Examples of ESF depletions reaching conjugate locations at midlatitudes were shown by Martinis and Mendillo (2007) where airglow depletions associated with ESF were observed at the Arecibo Observatory (L ~ 1.4), and also in the southern hemisphere at El Leoncito Observatory.

1.2. Emissions from sub-auroral latitudes to the geomagnetic equator

Airglow is the term for the photons emitted by atmospheric processes involving chemistry (Solomon and Abreu, 1989). The most common mechanism is dissociative recombination of ions and electrons

$$XY^+ + e^- \rightarrow X + Y^*, \quad (1)$$

where $*$ indicates an excited state that decays photoradiatively through

$$Y^* \rightarrow Y + \text{photon} \quad (2)$$

This type of emission has relevance to studies of plasma-neutral abundances in the upper atmosphere (~200–500 km).

All such emission effects in the upper atmosphere occur at all hours of local time, and thus Airglow = Dayglow + Nightglow. Dayglow is difficult to detect in the presence of bright sunshine, but observations can be made using specialized optical systems (see review by Chakrabarti, 1998). Nightglow is far easier to detect during the hours after sunset and prior to dawn. This is the emission type we discuss in this paper. For example, 630.0 nm airglow is emitted through the sequence

$$O_2^+ + e^- \rightarrow O + O^* \quad (3)$$

with O^* representing an oxygen atom in the ^1D excited state. Under the right conditions the O^* returns to the ground base state by emitting a photon in 630.0 nm:

$$O^* \rightarrow O + 630.0\ \text{nm photon} \quad (4)$$

Another emission that is used to study ionospheric processes is 777.4 nm. It results from the radiative recombination of oxygen ions

$$O^+ + e^- \rightarrow O^* \rightarrow O + 777.4\ \text{nm photon} \quad (5)$$

Nightglow from the ionosphere is rarely uniform over the field of view of an ASI system. Gradients in brightness describe plasma gradients over large distances. In addition to such large-scale effects, the ionosphere can contain dramatic spatial variations due to plasma dynamics, instabilities or waves, and these airglow structures appear as modulation patterns of the background airglow brightness. At middle latitudes, for example, MSTIDs appear as moving bands of bright and dark airglow. At equatorial and low latitudes, plasma instabilities associated with ESF with reduced ionospheric densities appear as large-scale *airglow depletions*—often with imbedded smaller structures and bifurcations that illuminate the complexities of the instability mechanism. At sub-auroral latitudes SAR arcs occur only during geomagnetic storms (Kozyra et al., 1997). While their origin depends upon energy input from the magnetosphere, the mechanism is not one of energetic particle precipitation or atmospheric chemistry. Oxygen atoms in the thermosphere are excited to their ^1D state by collisions with hot ambient electrons in the sub-auroral ionosphere

$$O + e^{-*} \rightarrow O^* + e^- \quad (6)$$

followed by photo-radiative decay

$$O^* \rightarrow O + 630.0\ \text{nm photon} \quad (7)$$

Airglow and SAR arcs are sub-visual emissions readily studied using two-dimensional imaging systems. For example, SAR arcs are most often narrow bands of emission in latitude (1–3°) extending in longitude from horizon to horizon. They are distinct emission features found only during geomagnetic storms (and thus typically a few nights per month) during active periods of the solar cycle. Current studies of SAR arcs deal with the mechanism(s) that heat ionospheric electrons, and those processes that result in heat conduction from the inner magnetosphere into the topside ionosphere.

Finally, in the Earth's mesosphere (~80–110 km), ionospheric densities are extremely low at night, and thus virtually all background airglow and any structures within it are due to neutral atmosphere dynamics (waves and tides) that produce bright and dark patterns of emission via chemical excitation and decay. Mesospheric science is enabled at each of our ASI locations, with location ranging from mountain top observatories to others at coastal and island locations. These various site conditions allow for different types of upward propagating sources to be detected within the mesosphere. There are no mechanisms in the mesosphere that relate to geomagnetic conjugate point physics. Nevertheless, we will include some mesospheric science issues that affect some aspects of the instrumentation to be described (e.g., filters, and duty cycle), while keeping the main focus and discussion to conjugate point science at thermosphere-ionosphere heights.

2. Instrumentation

There are two basic ways to record the two-dimensional patterns of airglow and any structures they might contain—rapidly scanning photometers and cameras with fish-eye lenses. While scanning photometers were developed first (e.g., Slater and Smith, 1981), they did not become the dominant form of 2-D imaging. They were superseded by 2-D imagers using intensified Vidicons, and later by charged coupled devices (CCDs).

One of the challenges of designing a wide angle (~180°), narrow band (~1.5 nm) imaging system is keeping the maximum angle that any ray may make with the normal to the surface of the filter to <5° or so. The requirement is necessary because the central wavelength (CWL) of an interference filter shifts towards shorter wavelengths with increasing angle of incidence. For most filters, a 5° angle will correspond to a ~0.5 nm shift of the CWL. The filter must have a bandwidth (BW) large enough (~1.5–2.0 nm) to accommodate this shift without causing a significant loss in Transmission (T) at the desired airglow wavelength. It is also desirable to have the filter treat the entire field of view (FOV) the same. To accomplish this, a lens is inserted just before the image plane of the fish-eye lens to make the axis of converging bundles of rays to be perpendicular to the filter surface. With the addition of such a lens, the system is said to be "telecentric".

The diameter of the image just behind the telecentric lens is ~85 mm, so the filters must be at least this size. The first generation ASIs built at Boston University (Baumgardner et al., 1993) used 100 mm dia. filters, so the filter wheels were made to accommodate this filter size. The detector used in this system is a 1024 × 1024 CCD with 0.013 mm pixels. With anti-reflection coatings and modern electronics, this CCD has a quantum efficiency (Q.E.) of ~90% (near 600 nm), and a read noise of ~3 electrons (RMS) (the noise equivalent of ~10 photo-electrons/pixel/read cycle). Using an Electron Multiplying CCD (EMCCD) this read noise can be reduced to essentially zero.

The 85 mm dia. image at the fish-eye lens is much too large to fit on the CCD (~13 mm × 13 mm) so a series of lenses is used to re-image it on to the CCD (see Fig. 1). The objective lens fitted to the CCD camera is a 50 mm f.l. F/0.95 high quality camera lens. Since the image must be minified by a factor of ~6.5 to fit onto the CCD, a second system of lenses is used to act as a collimator. The effective focal length (EFL) of this collimator must be 50 × 6.5 or ~325 mm (a 360 mm f.l. commercial camera objective is used so that when fitted with its own telecentric lens it has the appropriate EFL). The net result is a ~13 mm dia. image on the CCD at F/0.95. The collimator and, consequently, the fish-eye are being used at ~F/6. The max angle at the filter is: arctan(1/(2 * F/#)) or 4.76°. The actual aperture at the fisheye is ~0.5 cm, i.e., 30 mm f.l./F/#. To estimate the A-Omega product for the ASI we can use the fact that it images 2π steradians in a ~13 mm

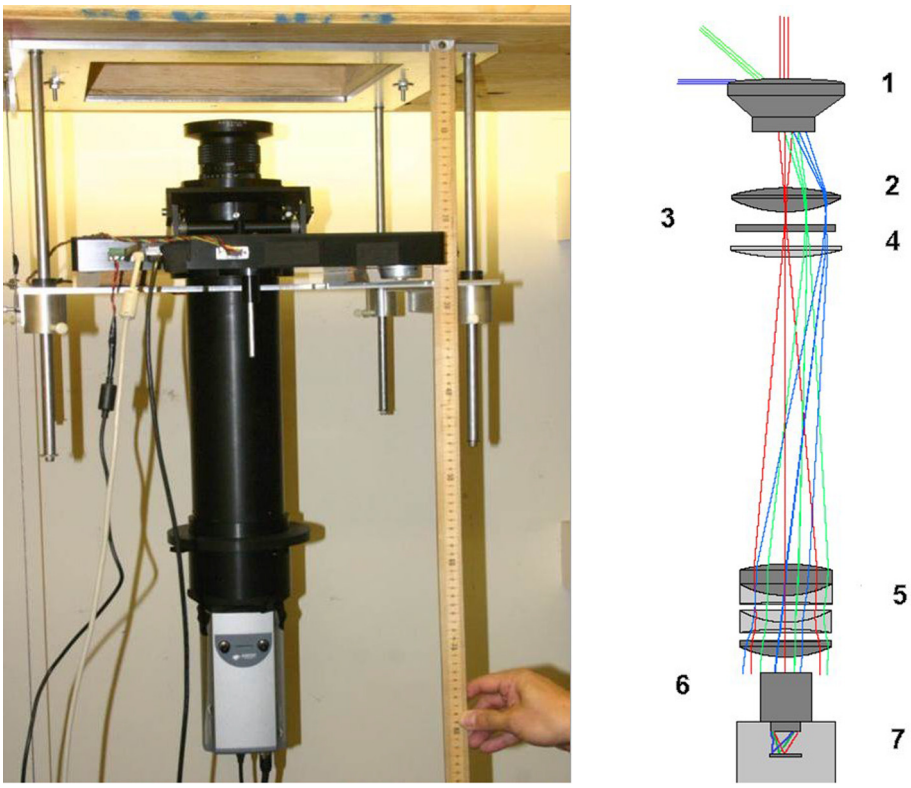

Fig. 1. (a) Example of the all-sky-imager (ASI) designed at Boston University for observations of emissions from the Earth's upper atmosphere. The thin rectangular section, just under the fish-eye lens, is a 6 position filter wheel housing. The ASI also includes a mechanism for setting an optimal focus for each filter being used; (b) schematics showing how the light propagates through the optical the system: (1) 30 mm f.l. F/3.5 Arsat Fisheye; (2) 90 mm f.l. F/1.0 lens; (3) 100 mm dia. Filter ~1.5–2.0 nm HPFW; (4) 350 mm f.l. plano-convex lens; (5) 360 mm f.l. F/4.5 Tessar; (6) 50 mm f.l. F/0.95 Senko lens; and (7) 1024 × 1024 CCD with 0.013 mm pixels.

(1024 pixels) diameter circle (the actual measured image diameter is ~11.5 mm or 885 pixels). This gives a value of $\sim 1.0 \times 10^{-5}$ ster/pixel. The area of the aperture is ~0.2 cm^2, therefore the A-Omega product is: $\sim 2 \times 10^{-6}$ cm^2 Steradians. The normal operating mode of the ASI's is to bin the CCD 2 × 2, so the A-Omega is 8×10^{-6} cm^2 Ster. To estimate the throughput of the system the transmission of the optics and the filter must also be known and are a function of the wavelength being measured. A conservative estimate for the ASI at 630 nm is T = 0.30 (including the 75% T for the filter).

An alternative detector system is available for the ASI that uses a 2048 × 2048 × 0.013 mm pixel CCD. This alternative camera is fitted with a 100 mm F/1.0 lens. This camera system uses almost all the available aperture of the fisheye and yields an increase of a factor of ~3 in throughput (the max angle at the filter increases to ~7.5° requiring the filter BW to increase to 2.5–3.0 nm).

3. Calibration and image processing

3.1. Brightness calibration

When all-sky cameras were first used to observe aurora, they were 'white-light' systems that captured the positional and temporal patterns of the aurora being studied. There was little concern about specifying the quantitative brightness levels captured in such visible light systems. Prior to the use of digital detectors being used in ASIs, photoelectric photometers and spectrometers were the main instruments used for quantitative measurements of the nightglow. Since the nightglow always filled the field of view of these instruments, the methods used for characterizing the brightness of stars by photoelectric photometry was found to be not very useful for the airglow. Hunten et al. (1956) proposed a new unit of brightness, the Rayleigh (R), that has units directly relatable to the physical processes in the airglow layer producing the photons, where: $1R \equiv 10^6$ photons/cm^2/sec/4π ster, or $1R = 7.96 \times 10^4$ photons/cm^2/sec/ster. For example, a 10 km thick airglow layer having a uniform volume emission rate of 1 photon/sec/cm^3 would be said to have a brightness of 1R.

Today, simply specifying the temporal-spatial characteristics of airglow structures is insufficient for the science topics being studied. Understanding the physics of emission requires knowing the brightness (in Rayleighs) observed. Descriptions of the calibration methods used for Boston University designed all-sky-imagers and meridional imaging spectrographs were given in Baumgardner et al. (2007).

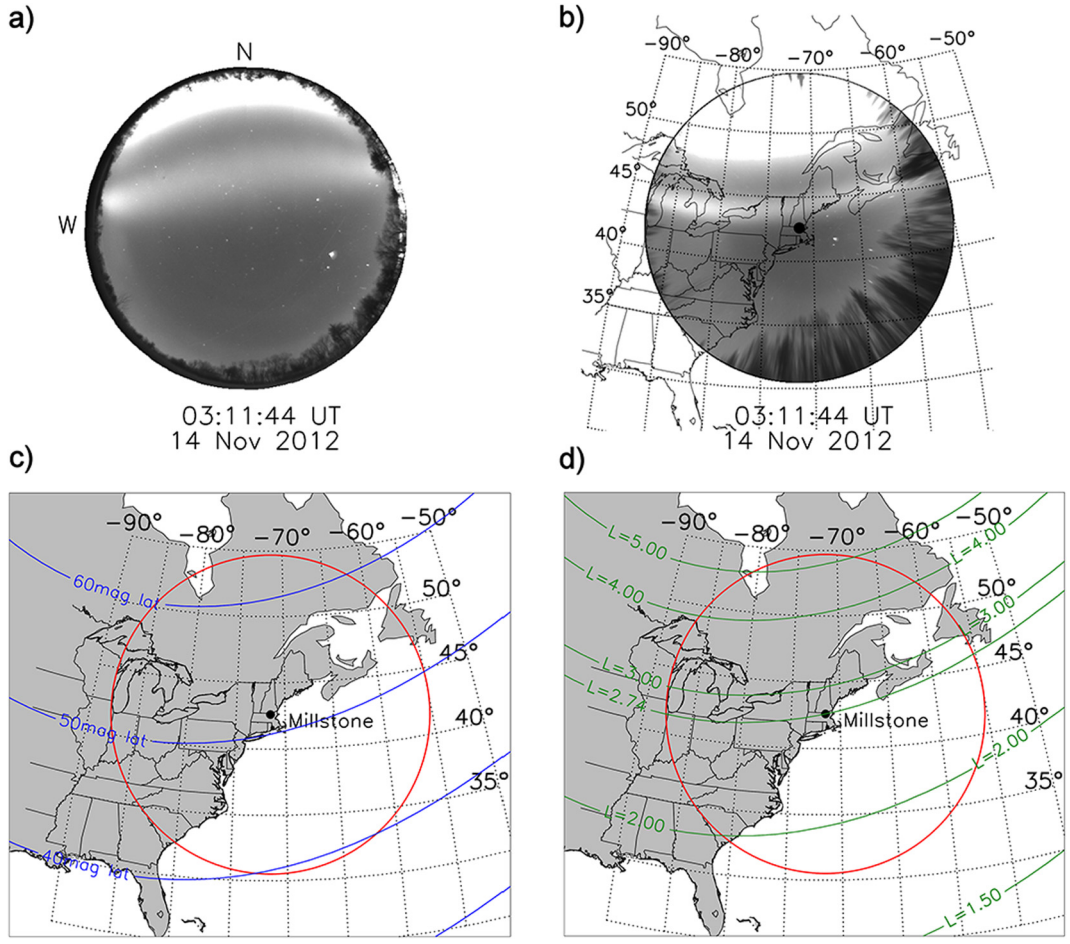

Fig. 2. A stable auroral red (SAR) arc in (a) raw data format, and (b) "unwarped" upon a geographic map for an assumed emission altitude of 400 km. The field of view represented here is 160°; c) The range of geomagnetic latitudes within the 160° FOV and (d) their respective *L* values (magnetic field line distance in the geomagnetic equatorial plane) (from Mendillo et al., 2016).

Once the ASIs are deployed, they rarely come back to the lab for repair or re-calibration (however, the interference filters are periodically re-measured for any drift in the CWL). Therefore, the brightness calibration techniques presented in Baumgardner et al. (2007) have been augmented with additional methods based on data taken in the field rather than depending on laboratory measurements alone. This field method is based on measuring the total brightness in Data Numbers (DN) of stars of known flux (photons/cm^2/sec/nm) throughout the night, removing the known vignetting function of the instrument, and then plotting these DN values (normalized by the star's flux) vs the zenith distance of the star. Such a plot shows the gradual extinction of the starlight as they approach the horizon (Martinis et al., 2013). This extinction curve can also be used to evaluate the amount of tropospheric scattering on this night. A curve is fitted to this data, and when combined with the known filter parameters (the area under the filter transmission curve in nm), a responsitivity factor (Rayleighs/DN.sec) can be derived. Only very clear (photometric) nights are used for this calibration. This technique will account for any loss of transmission of the ASI that may arise because of dust, dew, etc., covering the fish-eye lens or dome. The responsivity factors obtained are typically within 20% of the values obtained in the lab with a C14 standard source. Another source of uncertainty is related to tropospheric conditions that will scatter photons into or out of the field of view, e.g., haze, thin clouds, etc. Some of the data (x, y pixel locations, elevation (El) and azimuths (Az)) gathered during this star calibration procedure are also used to characterize the distortion present in the all-sky image and to determine the orientation of the instrument so that the image data can be placed in a georeferenced context. This procedure is detailed next.

3.2. Geometrical image processing

Separate from the brightness calibration methods for ASI images described above, here we summarize ASI data presentation methods that enable scientific analyses of those images. Raw data are taken using a fisheye lens that captures emission patterns versus elevation angle (El) and azimuth (Az). These are not the most useful coordinates for geophysical interpretation, nor for comparisons with other data sets (e.g., line-of-sight radars or satellite passes). There is only a quasi-linear relation between the El value

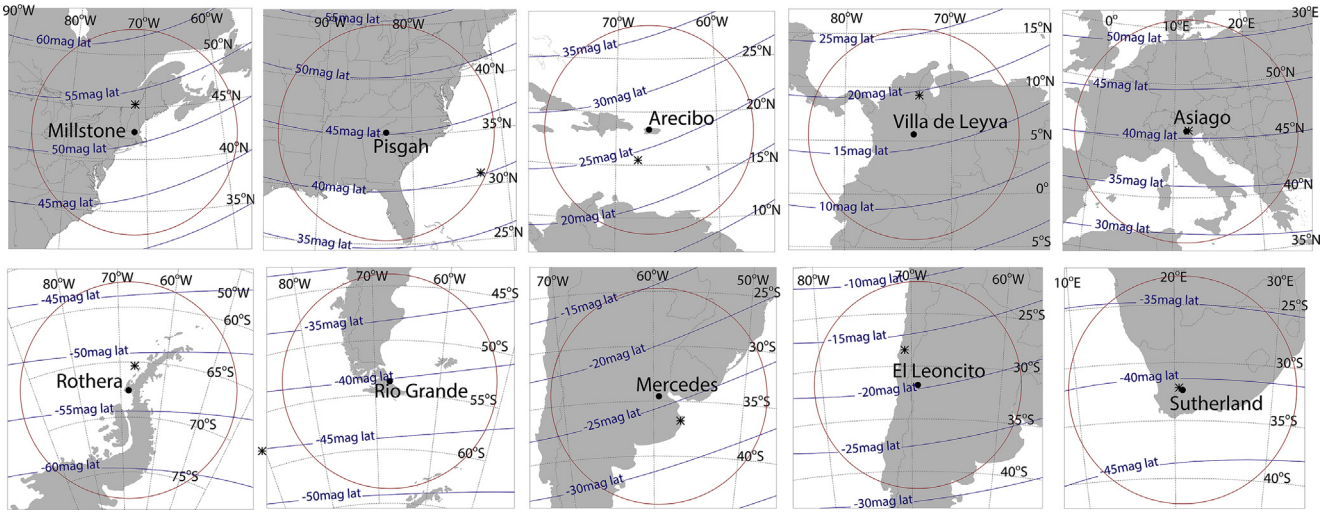

Fig. 3. Five sets of field-of-view (FOV) maps using a 300 km emission height and zenith angle down to 80°. (a) Millstone Hill – Rothera, (b) Pisgah – Rio Grande, (c) Arecibo – Mercedes, (d) Villa de Leyva – El Leoncito, and (e) Asiago – Sutherland. For each FOV, the dot gives the local zenith and the asterisk gives the location of that station's conjugate point zenith mapped along the B-field line from the opposite hemisphere.

and radial distance of a pixel in an all-sky image, with considerable compression at lower El values. We call these raw images "warped" images. Yet, each pixel has a pair of specific El and Az values that correspond to a unique latitude and longitude if the height of emission is assumed. A significant body of literature has dealt with 6300 Å emission height issues, ranging from tomographic/triangulation of observations to compute emission layer characteristics (e.g., Semeter et al., 1999), sounding rocket observations of emission versus altitude (Semeter et al., 1996), to models of emission profiles (Rees and Roble, 1975, 1986). Each emission process of course occurs over a range of altitudes, and so by emission height we mean average height for a specific emission layer. The consensus for the 6300 Å wavelength used in our ASI systems is as follows: 200 km for diffuse aurora, 300 km for airglow, and 400 km for SAR arcs. When 7774 Å emissions are used, their emission height is also ~400 km (or the height of the peak of the F2 layer (hmF2)). Filters used for mesospheric studies, e.g., sodium and OH emissions, have emission heights of ~90 km. Finally, oxygen's 5577 Å emission can come from three distinct regions: the mesosphere at ~95 km; auroral processes at ~120 km, and thermospheric heights of ~300 km. Once the appropriate height of the emission in question is chosen, an "un-warped" version of the all-sky image can be made where now each pixel in the original (warped) all-sky image now has a geographic latitude and longitude and placed on a map centered on the observation site.

Depending on the assumed emission height, and the zenith distance used (typically 75 or 80°) this map can cover a region as large as ~2000 km in diameter (e.g. a SAR arc at 400 km) or only 800 km for mesospheric (~90 km) emissions.

As an example of these methods, we show in Fig. 2 a SAR arc event of 14 November, 2012. A typical all-sky raw (warped) image appears in Fig. 2a. After assuming an average emission height (e.g., 400 km for a SAR arc) we associate each pixel at a given Az and El with a geographic latitude and longitude. The result of such a mapping is called an unwarped image (Fig. 2b). To specify the geophysical context of an image, it is useful to overlay the image with geomagnetic coordinate grids. For SAR arcs, the parameter most relevant to inner magnetosphere morphologies is the L-shell value (McIlwain, 1961) related to geomagnetic latitude, obtained using Magnetic Apex coordinates (Richmond, 1995). Fig. 2c and d indicates the range of magnetic latitudes and L values, respectively, at 400 km.

In Fig. 3, for each of the stations that form conjugate point pairs, we show the FOV at 300 km with zenith indicated by circles and the conjugate point zenith mapped along the field line from the opposite hemisphere by asterisks. Magnetic latitudes are indicated in blue.

The network of ASIs can also be used to investigate longitudinal variability. For example, the two pairs of subauroral stations Millstone Hill and McDonald Observatory can be used to map SAR arcs across vast regions. For example a SAR arc at L = 2.5 (and an emission height of 400 km) appears near zenith at Millstone Hill, but to the north at McDonald. Similarly in the Southern Hemisphere, the Mercedes and El Leoncito ASIs, covering a longitudinal range of ~40°, allow us to track the evolution and zonal motion of airglow depletions associated with ESF and the northwestward motion of MSTIDs. Fig. 4 shows a composite image using McDonald and Millstone Hill ASIs during the 1 June, 2013 storm. The McDonald results, showing the intrusion of low latitude airglow depletions associated with ESF to the south, MSTIDs to the North West, and auroral features to the North were discussed in Martinis et al. (2015). Here we added a simultaneous image from Millstone Hill that shows clearly a

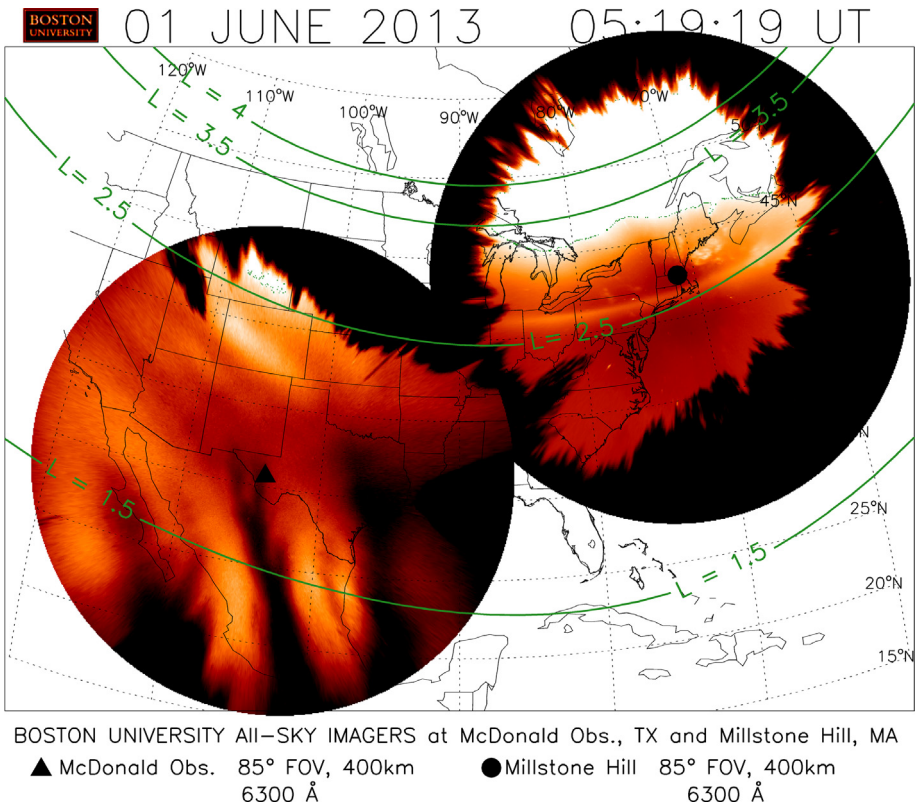

Fig. 4. Simultaneous images from Millstone Hill and McDonald Observatory showing SAR arcs at both sites, while ESF and MSTIDs are observed only at McDonald. These stations share common geomagnetic latitudes (and L-values) that can be used to describe the spatial consistency or disparity over a longitude range of ~60° of longitude.

strong aurora to the north and a bright SAR arc near zenith at $L \sim 2.5$. Trees near the northern horizon at McDonald prevent the observation of the entire arc at $L \sim 2.5$.

4. Site requirements, data taking, transfer and archiving

4.1. Sites

Each of the Boston University ASI instruments is an autonomous observing facility. In all cases, the pairing of stations to form conjugate point capabilities started with a primary site (e.g., Millstone Hill, Arecibo, El Leoncito, Rio Grande, Asiago), and then an appropriate conjugate point match was found (Rothera, Mercedes, Villa de Leyva, Pisgah, Sutherland). At each of the sites, an observing room with access to a dome had to be found, or a small building was constructed to meet our needs. Beyond physical housing, the primary criteria at each site were dark skies, favorable horizon (to ~75° zenith angle) in all directions, high-speed internet connection, environment control (i.e., temperature and humidity within the observing building), and on-site technical staff for occasional service requests. For non-US sites (Argentina, Peru, Colombia, Italy, South Africa, New Zealand and Antarctica), the logistics of shipping technical equipment encountered site-by-site differences in export/import controls and customs regulations that were neither minor in costs nor in time and effort. Strong collegial support from our hosts was always the over-arching enabling factor for success.

4.2. Data taking, transfer and archiving

Each ASI is assigned a yearly schedule of operations that is uploaded to its on-site computer via control from our Imaging Science Laboratory in Boston. Thus, operations can be monitored or changed by an on-site staff member or from Boston. Typically, each system operates between the astronomical twilights (SZA $< -12°$) of sunset and dawn—essentially an hour after ground sunset to an hour before ground sunrise. The days of full moon ($\pm$ two adjoining days) are removed from the schedule to avoid unfavorable imaging conditions. Nights of gibbous phase moon have shorter observing periods as well.

Each ASI system has a filter wheel with six options that are typically assigned to the following wavelengths (557.7 nm, 630.0 nm, 777.4 nm 589.3 nm, >695.0 nm, and 605.0 nm or 644.4 nm). Table 1 shows a summary of the species and heights involved for the different emissions. The integration time for each filter and the duty cycle for the full set of operations can be adjusted for either routine data-taking or campaign-mode observations. The standard

Table 1
Filters and species involved in a typical all-sky imaging system.

Filter (nm)	Species	Height
557.7	O (^{1}S)	Mesosphere; thermosphere/ionosphere
630.0	O(^{1}D)	Thermosphere/Ionosphere
777.4	O(^{5}P)	Ionosphere
589.3	Na (D1 + D2)	Mesosphere
>695.0	OH	Mesosphere
605.0 or 644.4	–	Background/ambient

practice is to use 2-min integrations and thus a 12-min cycle for all filtered images.

Throughout a night's observations, the images are stored on the computer that controls ASI operations, then are transferred to Boston via secure FTP (SFTP) each day after data-taking has ended. All observations are archived permanently in Boston and are made accessible to the research community and general public at the website www.buimaging.com, generally within 12 h. The data undergo minimal processing prior to their availability, such that images are dark subtracted, oriented with north at the top, and an empirically determined brightness-scaling algorithm is applied in order to facilitate feature identification. A user-friendly menu guides data viewing and comparison. For example, at each site the periods of observation are sorted by wavelength and year and displayed using a calendar interface. Quick look movies and all individual images are shown, and comparisons can be made with other wavelengths at the same site or for same wavelengths at another site (e.g., its conjugate point). The COSPAR and international communities in Space science are encouraged to use our data base for independent and/or collaborative studies.

5. The Boston University ASI network

Boston University's first all-sky camera designed for ionospheric research was the system described in Mendillo and Baumgardner (1982) for use in campaign-mode equatorial aeronomy research. The detector used was 35 mm black-and-white film. Within a few years, the new charge-coupled-device (CCD) detector system became available and this was used for Boston University's first permanent ASI site on the grounds of the MIT Haystack Observatory in Westford, MA (42.5 N, 71.5 W), as described in Baumgardner and Karandanis (1984). Coordinated research using optical methods in conjunction the incoherent scatter radar (ISR) at Millstone Hill/Haystack followed (Mendillo et al., 1987). The extension of ASI-plus-ISR approach occurred in 1993 with the installation of a Boston University ASI system at the Arecibo Observatory in Puerto Rico (Mendillo et al., 1997a), and then in Arequipa, Peru to operate in conjunction with the Jicamarca ISR (Mendillo et al., 1997b).

Support for additional optical science instruments came when the US National Science Foundation introduced its Coupling, Energetics and Dynamics of Atmospheric Regions (CEDAR) program to foster the "chains and clusters" approach of diagnostic instruments.

Significant resources also became available from the US Department of Defense initiative called the Defense University Research Instrumentation Program (DURIP), with its space physics grants administered by the Office of Naval Research and the Air Force Office of Scientific Research. Using these programs over a multi-decade period, the current distribution of Boston University ASI sites is shown in Fig. 5, with site specific locations summarized in Table 1. We now review briefly the primary research agenda for each conjugate-point pair of stations.

5.1. Site selection based on science objectives: equatorial and low latitudes

The most dramatic class of ionospheric disturbances in the geospace environment are the plasma irregularities associated with the Gravitational Rayleigh-Taylor Instability at equatorial and low latitudes (Kelley, 2009). These disturbances were first encountered when ionosondes at low latitudes suffered signal degradation in attempts to detect clean reflections from the ionospheric F-layer. The spreading of returned signals (both in frequency and reflection altitude) led to the name equatorial spread-F (ESF). This term has survived for decades, in conjunction with alternate designations from different diagnostic systems. For example, an ESF event observed by an incoherent scatter radar is in the form of *plumes* of back-scattered signals. An *in-situ* instrument on a satellite orbiting within the ionosphere sees an ESF event as a *plasma bubble* containing strongly fluctuating small scale-irregularities. A radio signal from a GPS satellite encountering an ESF event see it as a line-of-sight total electron content *depletion* with amplitude and phase *scintillations*. ESF plumes, bubbles and depletions all appear in the airglow layers between ~250–300 km (for 630.0 nm) and at ~400 km (for 777.4 nm), and thus an ASI system records ESF as an *airglow depletion*. The vast extent of ESF effects determined from images of airglow depletions was first achieved using the ASI system on the airborne observatory of the Air Force Cambridge Research Laboratory (AFCRL). This unique capability for campaign mode missions established the optical role in ESF research (Weber et al., 1978; Moore and Weber, 1981). The first ground-based use of an ASI system for ESF science was conducted in campaign-mode experiments from Ascension Island (Mendillo and Baumgardner, 1982; Mendillo and Tyler, 1983). Makela (2006) presented a review of the optical imaging of low-latitude irregularity processes. That study recognized several outstanding questions, including seeding mechanisms, latitudinal dependence of zonal drifts of depletions, and inter-hemispheric mapping of small-scale structures. Otsuka et al. (2002) conducted geomagnetic conjugate observations from Japan and Australia and reported a single night with simultaneous observations. The results

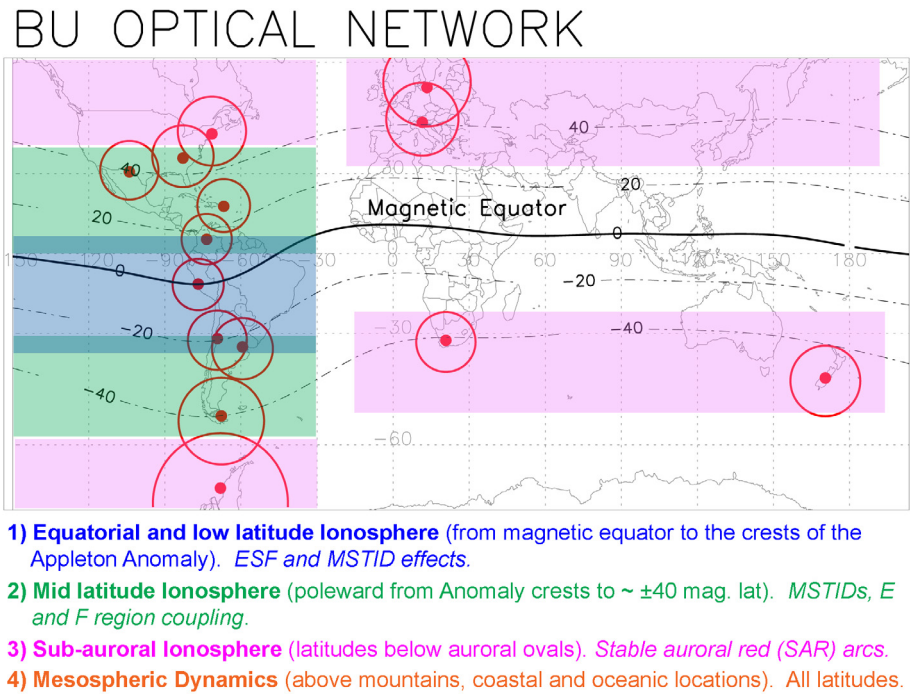

Fig. 5. The Boston University network of all-sky-imagers for upper atmosphere science in three latitude regimes. The circles show the fields-of-view for 630.0 nm emission height at 75° zenith angle. The ASIs in Antarctica, Germany, and North Carolina, US, are operated by the British Antarctic Survey/ Utah State University, the Leibniz Institute of Atmospheric Physics, and SRI International, respectively.

showed large scale ESF structures coinciding closely. Today, ASI systems are used to study ESF at various locations across the globe (Shiokawa et al., 2015; Sharma et al., 2014; Takahashi et al., 2015; Hickey et al., 2015).

As shown in Fig. 5 and Table 2, the Boston University network of ASI systems was configured to have a site at the geomagnetic equator (Jicamarca, Peru) plus two conjugate point sites at low magnetic latitudes in each hemisphere in the same longitude region—El Leoncito (Argentina) and Villa de Leyva (Colombia). Fig. 6 gives an example of airglow depletions using a set of simultaneous images in 777.4 nm emission at each site. As antici-

Table 2
Summary of observing site coordinates and their conjugate points for an emission height of 300 km.

Site	GLat[a]	GLon[b]	L-shell[c]	QDLat[d]	QDLon[e]	GLat_Conj[f]	GLon_Conj[g]	Conj. site
Millstone	42.64	−71.45	2.64	50.94	8.03	−65.07	−66.48	Rothera
Pisgah[1]	35.20	−82.88	2.10	45.02	−7.99	−58.10	−90.08	Rio Grande
McDonald	30.67	−104.02	1.74	39.09	−35.24	−46.51	−119.95	None
Arecibo	18.30	−66.80	1.30	26.31	11.05	−36.05	−56.75	Mercedes
V.Leyva	5.60	−73.52	1.13	16.09	1.16	−27.98	−70.51	El Leoncito
Jicamarca	−11.95	−76.87	1.05	−0.24	−3.96	−11.45	−76.89	None
El Leoncito	−31.80	−69.30	1.18	−19.84	2.07	9.67	−73.20	V.Leyva
Mercedes	−34.51	−59.40	1.26	−24.28	9.19	15.74	−68.02	Arecibo
Rio Grande	−53.79	−67.75	1.80	−40.35	5.02	31.47	−72.98	Pisgah
Rothera[2]	−67.50	−68.10	2.92	−53.22	7.74	44.90	−71.81	Millstone
Mt John	−43.99	170.46	2.62	−50.78	−104.54	54.10	−167.71	None
Asiago	45.87	11.53	1.82	40.68	87.09	−32.31	20.31	Sutherland
Sutherland	−32.37	20.81	1.82	−40.73	87.56	45.91	12.06	Asiago
Kuhlungsborn[3]	54.15	11.74	2.56	50.23	88.96	−45.60	30.08	None

[a] Geographic latitude.
[b] Geographic longitude.
[c] L-shell value.
[d] Magnetic latitude.
[e] Magnetic longitude.
[f] Conjugate geographic latitude.
[g] Conjugate geographic longitude.
[1] Operated by SRI International.
[2] Operated by Utah State University/ British Antarctic Survey.
[3] Operated by Leibniz Institute of Atmospheric Physics.

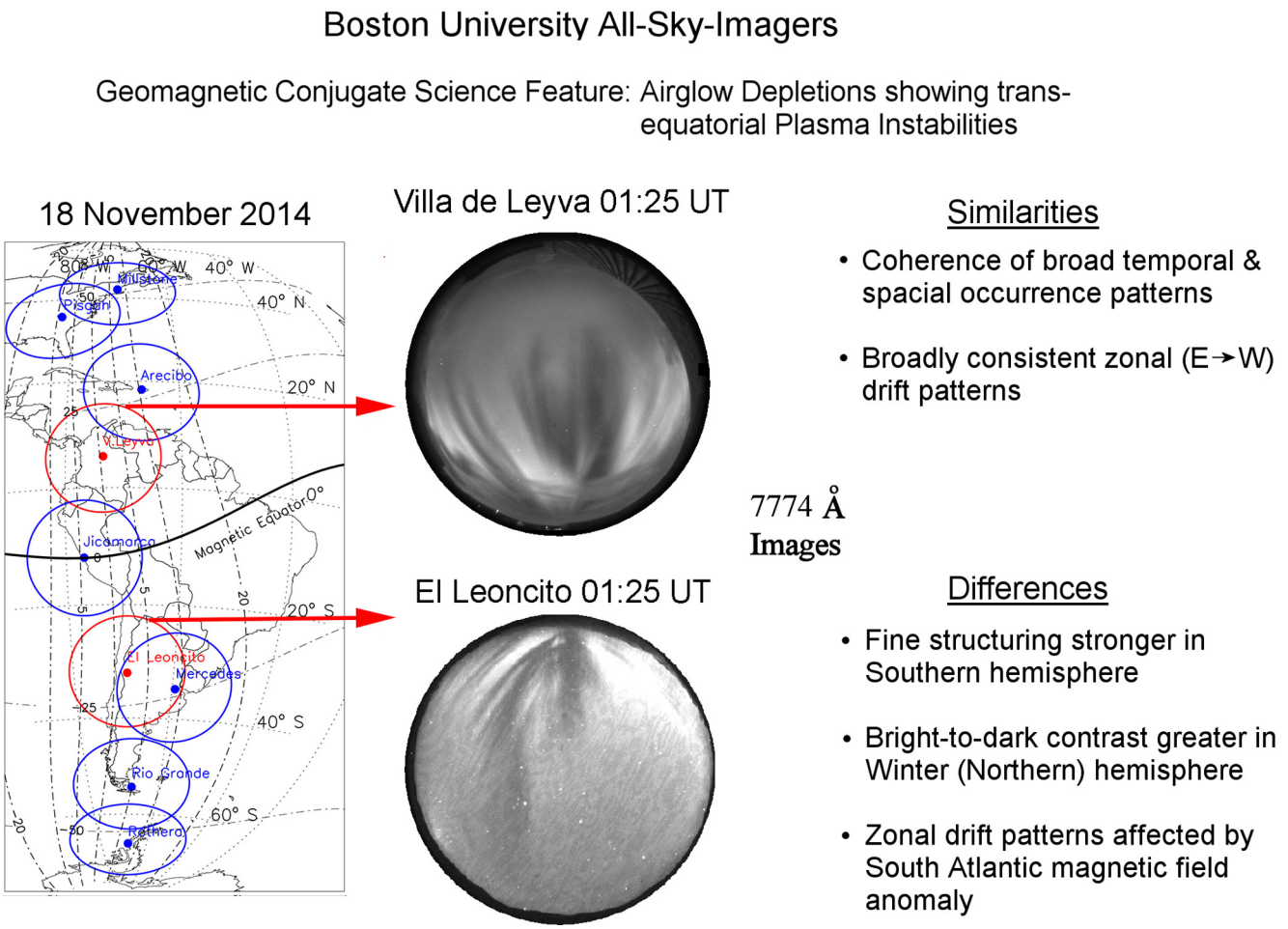

Fig. 6. ASI images in 7774 Å that show airglow depletions observed simultaneously (01:25 UT) from conjugate point observatories in Villa de Leyva (Colombia) and El Leoncito (Argentina).

pated, there are similarities and differences between the conjugate point images, as summarized briefly in the right side of the figure. The differences result from geomagnetic fluxtube-integrated instabilities that include different seasonal "receptor" conditions at the base points of the **B**-field lines—winter in the north and summer in the south. Previous studies utilized data from El Leoncito only (e.g., Martinis and Mendillo, 2007; Martinis et al., 2009), showing how GPS radio amplitude and phase scintillations coincided with the airglow depletion locations. Inter-hemispheric mapping from one site to the other can now be used to test "now-casting" predictions for space weather effects from one hemisphere to the other.

Of particular note are the highly structured bifurcations of irregularities previously seen at single stations—Ascension Island (Mendillo and Tyler, 1983) and Kwajalein (Mendillo et al., 1992, 2005). Bifurcation onsets typically occur at altitudes around 700 km. As can be seen in Fig. 6, the structuring on the night of 18 November, 2014 is far more extensive in the south. This type of difference in small-scale structuring for the same ESF event seen at opposite ends of the same ESF flux tubes has not been reported until now. The Otsuka et al. (2002) study had shown that the structures were identical in both hemispheres. We are in the process of assembling a more extensive set of examples to address the consistency of such effects, their possible causes, and space weather impacts upon GPS systems.

The availability of new conjugate point imaging data sets at low latitudes impacts the study of the coupled altitude-latitude extent of ESF fluxtubes. An airglow depletion's distance in latitude away from the geomagnetic equator relates directly to an ESF radar plume's extent in altitude above the equator (apex height). High altitude ESF patterns (with equatorial **B**-field apex heights > 1000 - sec km) were initially explained in terms of buoyancy physics (Mendillo et al., 2005). A dramatic case of ESF airglow depletions reaching the sub-auroral ionosphere (~40 mag latitude) questioned the extent of that mechanism (Martinis et al., 2015). The ESF event occurred during a moderate geomagnetic storm on 1 June, 2013 and was shown in Fig. 4. The high latitude/apex altitude reaching 7000 km (L ~ 2.1) was attributed to a combination of standard ESF disturbance upwelling augmented by solar-wind induced enhanced vertical drift (Martinis et al., 2015). It was also discussed that electric fields at the magnetic

equator at high altitudes mapped to midlatitudes creating the structures observed by the ASI at ~250–300 km (Martinis et al., 2016). With conjugate point ASIs now in both hemispheres, studies are underway dealing with space weather induced low-latitude "intrusions" into the mid-latitude domain.

Fig. 7 shows the first-ever set of three nearly simultaneous images of ESF airglow depletions spanning the geomagnetic equator to low latitudes in each hemisphere. This event on 30 October, 2014 provides visual evidence how this new resource can be used to study the latitude-altitude-temporal relationships between 630.0 nm airglow depletion signatures and ionospheric irregularities that cause radio disruptions. In the left panel, two-minute exposures taken during the pre-midnight hours are shown. In the central image, taken on the magnetic equator, the N-S aligned airglow depletion through zenith shows the envelope where ionospheric irregularities are found. This dark feature "connects" to structured airglow depletions at higher latitudes to the north and south, indicating that an entire magnetic meridian would experience these irregularities. The magnetic conjugacy is evident with depletions extending to ±20° magnetic latitude. A second pair of conjugate airglow depletions are captured to the east, but their equatorial signature falls beyond the field-of-view of the equatorial station. The degree of structuring appears more pronounced in the northern hemisphere (local Fall) versus that in the south (local Spring). In all previous studies of ESF patterns, distinctions were made between solstice and equinox conditions versus longitude; here we have a case of differences in season at the same longitude.

In the right panel of Fig. 7, again, three nearly simultaneous post-midnight images on the same night are shown. A dark airglow depletion spans the image from the equatorial site (Jicamarca). No corresponding depletions are seen in the north and south imagers because they would have been too far to the west to be in the FOV of these instruments. The well-formed depletion seen at el Leoncito is not evident at Villa de Leyva. The absence of a depletion in the north could be due to different "receptor" conditions there, e.g., the local ionosphere was too high or too weak to produce sufficient airglow to provide the contrast needed to reveal the depletion. So, by sampling both hemispheres simultaneously, new insights can be gained that would have not been possible from observations from a single site. A movie showing the evolution and zonal motion of the ESF structures can be found in the Supplementary material.

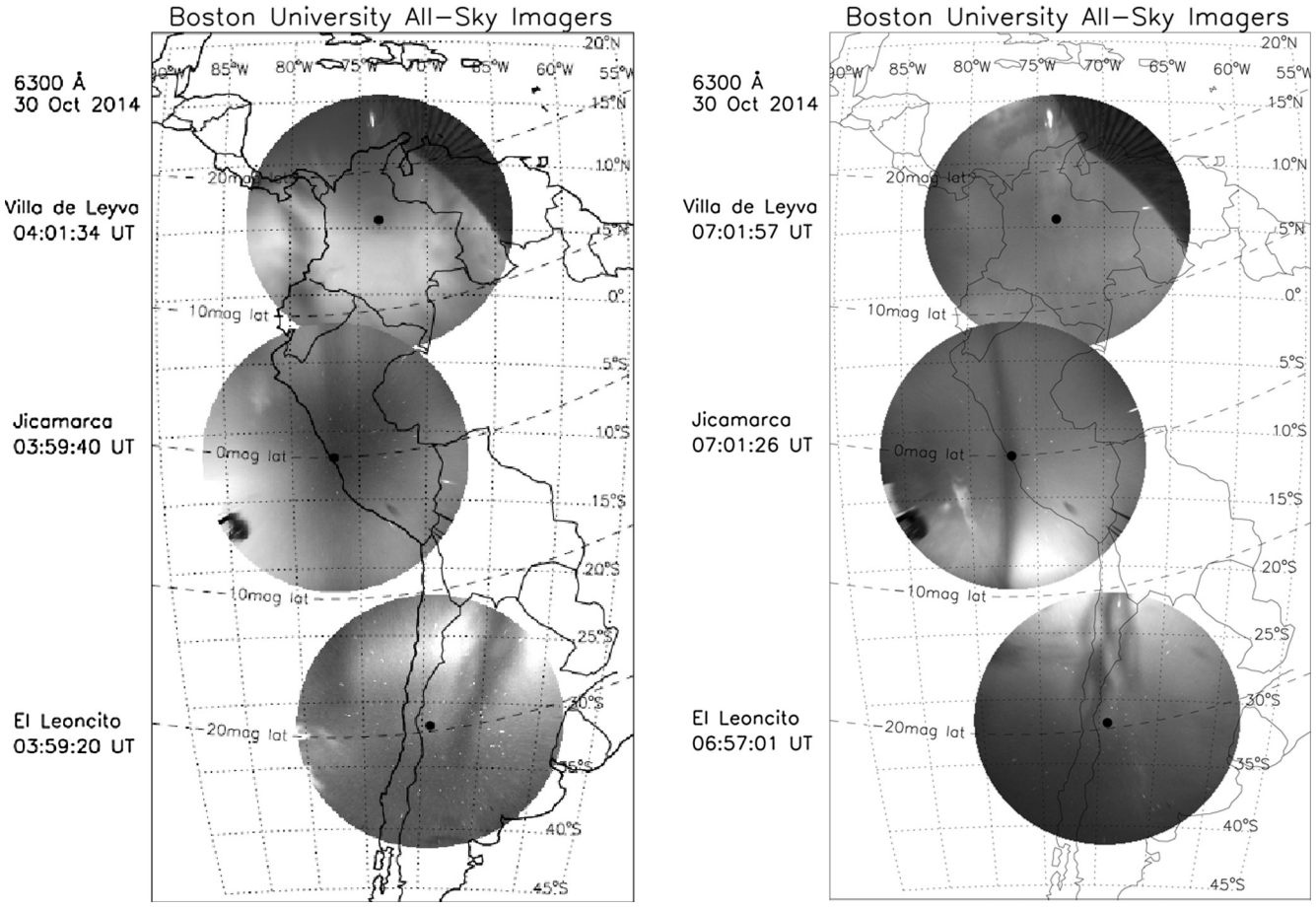

Fig. 7. Examples of three-site-FOV observations of airglow depletions on the night of 30 October, 2014. Panel (a) gives a pre-midnight sample and (b) a post-midnight set of images.

5.2. Site selection based on science objectives: middle latitudes

Incoherent scatter radar (ISR) observations at the Arecibo Observatory discovered unusual corrugations in ionospheric densities with horizontal scale size of 100's of kilometers (Behnke, 1979). The first optical studies of these mid-latitude structures were carried out using a BU ASI at the Arecibo Observatory (Mendillo et al., 1997b; Miller et al., 1997). That case study, and subsequent analyses (Garcia et al., 2000; Kelley et al., 2000), unified the ISR and ASI observations of medium scale travelling ionospheric disturbances (MSTIDs). The airglow signatures of an MSTID are bright and dark bands moving from northeast to southwest in the northern hemisphere. The first airglow observations of MSTID structures in South America occurred with the BU ASI at El Leoncito (Martinis et al., 2006). These features emerged from the SE and moved to the NW showing them to be hemispherically-coherent, electrodynamical phenomena. Studies in the Brazilian sector also showed band-like structures moving NW (Pimenta et al., 2008). They had high occurrence rates during June solstice months, but suffered from very few observations during December solstice months due to bad weather (Candido et al., 2008).

These studies prompted us to establish our site at Arecibo's conjugate point (Mercedes, Argentina), and Martinis et al. (2010, 2011) described the first simultaneous optical-GPS study of MSTID conjugate structures in the American sector.

Examples of conjugate point MSTIDs are given in Fig. 8. The format is the same as in Fig. 6 with similarities and differences noted—in this case contrasting seasonal differences between northern winter and southern summer. In exploring such receptor condition differences, the hypothesis that E-layer processes are linked to MSTID occurrence patterns, and their electro-dynamical coupling from one hemisphere to the other, are concepts in need of rigorous validation. A crucial parameter is electrical conductivity (σ). The E-layer's transition across the sunset hours involves not only reductions in electron density, but also changes in the mix of ions needed to calculate σ values (Schunk and Nagy, 2009). The onset of Sporadic-E (Es) events and different E-region instabilities (e.g., quasi-periodic echoes, Es layer instability) are thought to be more important as an enhancement mechanism.

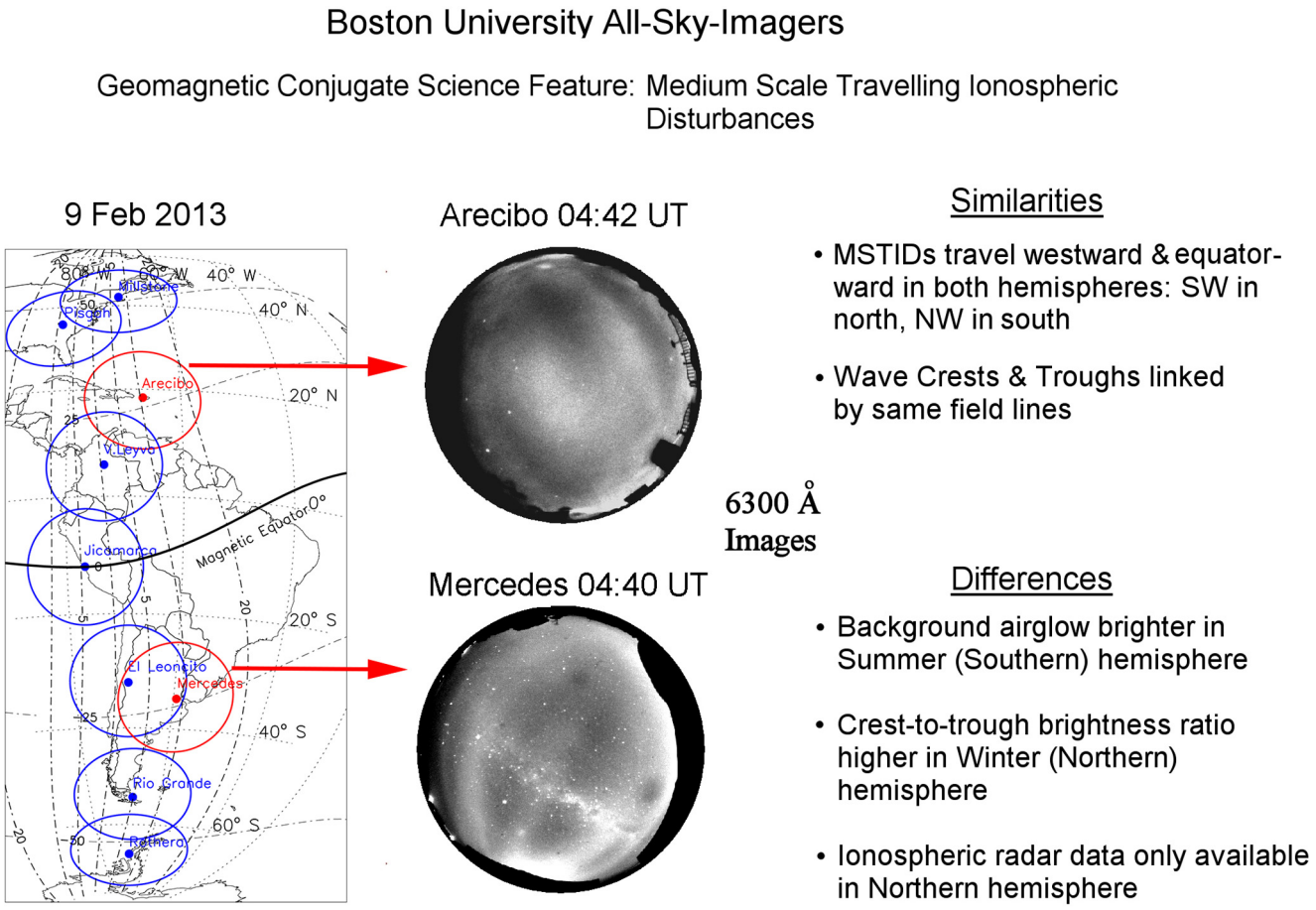

Fig. 8. Example of a Medium Scale Traveling Ionospheric Disturbance captured in 630.0 nm images from BU ASI systems at the Arecibo Observatory and the Mercedes Observatory (Argentina).

No long-term MSTID studies have been conducted using coordinated all-sky-imaging, radio (GPS and ionosonde) and satellite observations in the Europe-Africa sector, due mainly to the absence of the optical component. The promise of such work can be seen in the brief single-site imaging campaign (a few days in July 2002) conducted from the Greek island of Milos (Kelley et al., 2003). Our ASIs in Italy and South Africa remove that barrier and now MSTID conjugate-point research can be conducted in three longitude sectors (Pacific-American-European). Due to the tilt of the geomagnetic axis, there are strong differences between geographic and geomagnetic latitudes in the American versus Europe-Africa sectors. The influence of seasonal receptor patterns for such differences as well as potential differences in the direction of propagation, due to different magnetic declinations, can now be addressed.

5.3. Site selection based on science objectives: sub-auroral latitudes

The discovery of the SAR arc phenomenon was made in 1956 at the Haute Provence Observatory in southern France (Barbier, 1958, 1960). Within just five years, Roach and Roach (1963) presented a remarkably complete summary of existing observations and theories proposed to account for them. In quick fashion, Cole (1965) gave the now accepted explanation of a thermal energy excitation mechanism via geomagnetic field-aligned heat conduction from the magnetospheric ring current to ambient ionospheric electrons. These heated electrons subsequently impact atomic oxygen high in the thermosphere to yield spectrally-pure 6300 Å emission. The review paper by Hoch (1973) then summarized the status of a field barely 15 years old by linking optical observations made from the ground to the characteristics of the contracted plasmapause/ring current location observed in the inner magnetosphere. The final major contribution from the first two decades of SAR arc research appeared in the review paper by Rees and Roble (1975). In this classic for the field, they summarized past observations and occurrence patterns; more importantly, they presented the comprehensive formalism for calculating SAR arc emission rates from ambient ionospheric and thermospheric parameters that are readily observable.

Two solar cycles after the Rees and Roble (1975) review, Kozyra et al. (1993, 1997) re-energized the topic of SAR arc research. She conducted a far more in depth analysis of the physics of magnetosphere-ionosphere (M-I) coupling that links the ring current energy budget to the ionosphere-

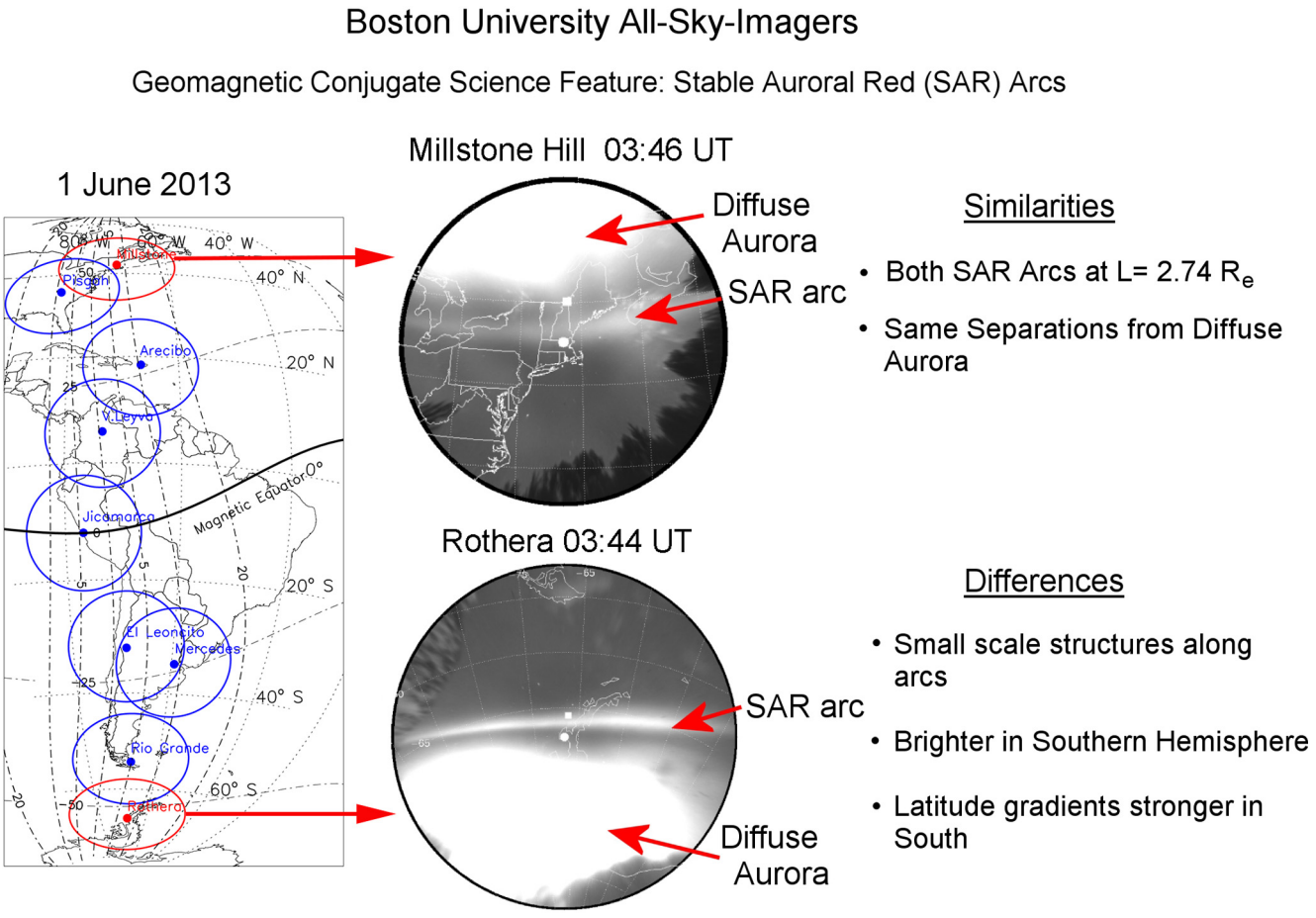

Fig. 9. Example of SAR arcs seen in conjugate point imagers at Millstone Hill and Rothera, Antarctica.

thermosphere system along the geomagnetic field lines that mark the location of the plasmapause. The seasonal effects in SAR arc occurrence and brightness levels were described and modeled, with emphasis on the roles played by receptor conditions in each hemisphere. This is precisely the topic that conjugate point observations can address. As shown in Fig. 5, there are three pairs of stations that can contribute to conjugate point studies of SAR arcs: Millstone Hill-Rothera, Pisgah-Rio Grande, and Asiago-South Africa.

Fig. 9 shows the first case of the same SAR arc imaged at conjugate locations. This was accomplished even though the conjugate pair Millstone-Rothera exhibits an extreme separation between geographic and geomagnetic latitudes that places unusual constraints upon simultaneous observing opportunities. At Millstone's latitude of 42.6°N, all-sky observations can occur throughout the year, from an hour after sunset to an hour prior to dawn. This "aeronomic window" can be as short as ~5 h during summer solstice and as long as ~11 h during winter solstice. At Rothera's latitude (68.1°S)—poleward of the Antarctic Circle—no summer (December solstice) operations are possible for months. Thus, when the Millstone system has its longest observing time (local winter), its conjugate instrument cannot be in service. This is not the case for SAR arcs in northern summer, as shown in Fig. 9. For this particular event, the summer (north) and winter (south) receptor conditions clearly led to different SAR arc morphologies for a given source region fixed in magnetospheric coordinates ($L \sim 2.7$).

The conjugate situation is much different with the ASIAGO (Italy)-SALT (S. Africa) pair of ASIs and the Rio Grande (Argentina) – Pisgah (North Carolina) pair. For example, the imager in Italy is at latitude 45.9°N, while its conjugate at SALT is located at 32.4°S. Observations can be made throughout the year. Their common magnetic latitudes are somewhat lower than the Millstone-Rothera pair, but clearly capable of detecting SAR arcs (Baumgardner et al., 2013). The Argentina-North Carolina pair can also capture SAR arcs when then appear at lower latitudes (stronger space weather events) in the ~70°W sector.

6. A new approach to study ionospheric plasmas

A network of conjugate point all-sky-imagers from the magnetic equator to sub-auroral regions (Fig. 5) has been deployed. Proof-of-concept results related to the goals of Space Weather research have been obtained (Figs. 6–9). We have found that the coherence of conjugate point results depends on the spatial scale of the phenomena being studied. Thus, features spanning large spatial scales appear morphologically similar at conjugate locations, although differences in contrast and sharpness can occur. At smaller scales, hemispheric differences can be quite substantial. Optical conjugate point science at middle and low latitudes offers a new method and therefore emerging opportunity to unify past single hemisphere results. Our goal is to investigate how the ionosphere behaves simultaneously in both hemispheres and to draw conclusions that could not be possible using single-site studies.

There are several points, common to all of the conjugate pairs of ASIs, that will guide future work:

* *How do the local "receptor" conditions of different seasons affect the same-source process being studied?* This is the over-arching goal of all conjugate studies.
* *How well do geomagnetic field models succeed in mapping effects observed in one hemisphere into the other hemisphere?* This is a fundamental aspect of all electrodynamical processes under investigation.
* *Can observations at one site be used to provide a "nowcast" of the same effect in the opposite hemisphere?* All-sky-imaging is the only diagnostic capable of providing a regional specification spanning ~1 million square kilometers every few minutes.
* *For nights when no disturbances are observed, can global circulation models (CGMs) successfully predict the background airglow observed in each hemisphere? Are empirical models of the ionosphere (e.g., the International Reference Ionosphere, IRI) and the thermosphere (MSIS) capable of successful airglow predictions in each hemisphere?* Calibrated emissions in Rayleighs (R) for 7774 Å observations depend on the accuracy of the electron density profile $N_e(h)$, while the emission at 6300 Å depends on a combination of $N_e(h)$ and neutral composition (O, O_2 and N_2) versus height.

Within this global approach, there are focused goals for each specific process—SAR arcs, MSTID, ESF effects—as summarized briefly in the "similarities" and "differences" shown in the first-results images (Figs. 6, 8 and 9) above.

Finally, the BU ASI Network will be used in conjunction with upcoming NASA missions. The GOLD (Global-scale Observations of the Limb and Disk) mission will be launched early 2018. It consists of a high-resolution far-ultraviolet imaging spectrograph with two identical channels that will be hosted on a commercial communications satellite (Eastes, 2009). It will sample the American sector from pole to pole from a geostationary orbit. One of the science questions the mission will address is related to the behavior of nighttime equatorial ionization anomaly (EIA) crests and ESF structures. The BU ASIs will be a crucial diagnostic component that provides ground-based support to identify the high-resolution structures associated with ESF and the EIA that are not capable of being viewed from orbit. Another NASA mission, ICON (Ionospheric Connection Explorer) will sample the ionosphere in a 27° inclination, 575 km circular orbit (Rider et al., 2015). One of the observing modes will measure simultaneously neutral winds at conjugate points in both hemispheres. The distribution of BU's ASIs in the American sector is ideally suited to provide supporting context for ICON's measurements.

Acknowledgements

This work was supported, in part, by grants from the National Science Foundation (AGS-1123222, MM; AGS-1552301, CM; OPP-1246423, CM; AGS-1552045, JB), and the Office of Naval Research (N00014-16-1-2596, MM). The authors wish to acknowledge and thank the continuing assistance from the Directors and personnel at our host facilities across the globe.

Appendix A. Supplementary material

Supplementary data associated with this article can be found, in the online version, at http://dx.doi.org/10.1016/j.asr.2017.07.021.

References

Abdu, M., Batista, I., Reinisch, B., de Souza, J., Sobral, J., Pedersen, T., Medeiros, A., Schuch, N., de Paula, E., Groves, K., 2009. Conjugate point equatorial experiment (COPEX) campaign in Brazil: electrodynamics highlights on spread-F development conditions and day-to-day variability. J. Geophys. Res. 114 (A4), A04308. http://dx.doi.org/10.1029/2008JA013749.

Akasofu, S.-I., 2003. Exploring the Secrets of the Aurora. Kluwer Academic Publishers, Dordrecht, ISBN 1-4020-0685-3.

Barbier, D., 1958. L'activite aurorale aux bass latitudes (Auroral Activit at low latitudes). Ann. Geophys. 14, 334–355.

Barbier, D., 1960. L'arc auroral stable (Stable Auroral arc). Ann. Geophys. 16, 544–549.

Baumgardner, J., Flynn, B., Mendillo, M., 1993. Monochromatic imaging instrumentation for applications in aeronomy of the earth and planets. Opt. Eng. 32, 3028–3032.

Baumgardner, J., Karandanis, S., 1984. CCD imaging system uses video graphics controller. Electron. Imaging 3, 28–31.

Baumgardner, J., Wroten, J., Semeter, J., Kozyra, J., Buonsanto, M., Erickson, P., Mendillo, M., 2007. A very bright SAR arc: implications for extreme magnetosphere-ionosphere coupling. Ann. Geophys. 25, 2593–2608.

Baumgardner, J., Wroten, J., Mendillo, M., Martinis, C., Barbieri, C., Umbriaco, G., Mitchell, C., Kinrade, J., Materassi, M., Ciraolo, L., Hairston, M., 2013. Imaging space weather over Europe. Space Weather 11, 69–78. http://dx.doi.org/10.1002/swe.20027.

Behnke, R.A., 1979. F layer height bands in the nocturnal ionosphere over Arecibo. J. Geophys. Res. 84, 974–978.

Burke, W.J., Martinis, C.R., Lai, P.C., Gentile, L.C., Sullivan, C., Pfaff, R.F., 2016. C/NOFS observations of electromagnetic coupling between magnetically conjugate MSTID structures. J. Geophys. Res. Space Phys. 121, 2569–2582.

Candido, C., Pimenta, A.A., Bittencourt, J.A., Becker-Guedes, F., 2008. Statistical analysis of the occurrence of medium-scale traveling ionospheric disturbances over Brazilian low latitudes using OI 630.0 nm emission all-sky images. Geophys. Res. Lett. 35, L17105. http://dx.doi.org/10.1029/2008GL035043.

Chakrabarti, S., 1998. Ground based spectroscopic studies of sunlit airglow and aurora. J. Atmos. Sol. Terr. Phys. 60 (14), 1403–1423.

Cole, K.D., 1965. Stable auroral red arc, sinks for energy of Dst main phase. J. Geophys. Res. 70, 1689–1706.

Eastes, R., 2009. NASA mission to explore forcing of earth's space environment. Eos Trans. AGU 90 (18). http://dx.doi.org/10.1029/2009EO180002, 155–155.

Eather, R., 1980. Majestic Lights: The Aurora in Science, History and the Arts. AGU, Washington, DC.

Frey, H., Mende, S., Vo, H., Parks, G., 1999. Conjugate observations of optical aurora with Polar satellite and ground-based camera. Adv. Space Res. 23 (10), 1647–1652.

Garcia, F., Kelley, M., Makela, J., Huang, C.-S., 2000. Airglow observations of mesoscale low-velocity traveling ionospheric disturbances at midlatitudes. J. Geophys. Res. 105 (A8), 18407–18415.

Hickey, D.A., Martinis, C.R., Rodrigues, F.S., Varney, R.H., Milla, M. A., Nicolls, M.J., Strømme, A., Arratia, J.F., 2015. Concurrent observations at the magnetic equator of small-scale irregularities and large-scale depletions associated with equatorial spread *F*. J. Geophys. Res. 120, 10883–10896. http://dx.doi.org/10.1002/2015JA021991.

Hoch, R.J., 1973. Stable auroral red arcs. Rev. Geophys. Space Phys. 11, 935–949.

Hunten, D.M., Roach, F.E., Chamberlain, J.W., 1956. A photometric unit for the airglow and aurora. J. Atmos. Terr. Phys. 8, 345–346.

Kalita, B., Hazarika, R., Kakoti, G., Bhuyan, P., Chakrabarty, D., Seemala, G., Wang, K., Sharma, S., Yokoyama, T., Supnithi, P., Komolmis, T., Yatini, C., Le Huy, M., Roy, P., 2016. Conjugate hemisphere ionospheric response to the St. Patrick's Day storms of 2013 and 2015. J. Geophys. Res. 121 (11), 11364–11390.

Kelley, M., 2009. The Earth's Ionosphere: Plasma Physics and Electrodynamics, second ed. Academic Press, New York.

Kelley, M., Haldoupis, C., Nichols, M., Makela, J., Belehadi, A., Shalimov, S., Wong, V., 2003. Case studies of coupling between the E and F regions during unstable sporadic-E condictions. J. Geophys. Res. 108 (A12), 1447. http://dx.doi.org/10.1029/2003JA009933.

Kelley, M., Makela, J., Saito, A., Aponte, N., Sulzer, M., Gonzalez, S., 2000. On the electrical structure of airglow depletion/height layer bands over Arecibo. Geophys. Res. Lett. 27 (18), 2837–2840.

Kozyra, J.U., Chandler, M.O., Hamilton, D.C., Peterson, W.K., Klumpar, D.M., Slater, D.W., Buonsanto, M.J., Carlson, H.C., 1993. The role of ring current nose events in producing stable auroral red arc intensifications during the main phase: observations during the September 19–24, 1984 equinox transition study. J. Geophys. Res. 98, 9267–9283. http://dx.doi.org/10.1029/92JA02554.

Kozyra, J.U., Nagy, A.F., Slater, D.W., 1997. High-altitude energy source (s) for stable auroral red arcs. Rev. Geophys. 35, 155–190.

Makela, J., 2006. A review of imaging low-latitude ionospheric irregularity processes. J. Atmos. and Sol. Terr. Phys. 68, 1441–1458.

Martinis, C., Baumgardner, J., Smith, S.M., Colerico, M., Mendillo, M., 2006. Imaging science at El Leoncito, Argentina. Ann. Geophys. 24, 1375–1385.

Martinis, C., Mendillo, M., 2007. ESF-related airglow depletions at Arecibo and conjugate observations. J. Geophys. Res. 112, A10310. http://dx.doi.org/10.1029/2007JA012403.

Martinis, C., Baumgardner, J., Mendillo, M., Su, S.Y., Aponte, N., 2009. Brightening of 630.0 nm Equatorial Spread-F airglow depletions. J. Geophys. Res. 114, A06318. http://dx.doi.org/10.1029/2008JA013931.

Martinis, C., Baumgardner, J., Wroten, J., Mendillo, M., 2010. Seasonal dependence of MSTIDs obtained from 630.0 nm airglow imaging at Arecibo. Geophys. Res. Lett. 37, L11103. http://dx.doi.org/10.1029/2010GL043569.

Martinis, C., Baumgardner, J., Wroten, J., Mendillo, M., 2011. All-sky imaging observations of conjugate medium scale traveling ionospheric disturbances in the American sector. J. Geophys. Res. 116, A05326. http://dx.doi.org/10.1029/2010JA016264.

Martinis, C., Wilson, J., Zablowski, P., Baumgardner, J., Aballay, J.L., Garcia, B., Rastori, P., Otero, L., 2013. A new method to estimate cloud cover fraction over El Leoncito observatory from an all-sky imager designed for upper atmosphere studies. Publ. Astron. Soc. Pacific 125 (923), 56–67.

Martinis, C., Baumgardner, J., Mendillo, M., Wroten, J., Coster, A., Paxton, L., 2015. The night when the auroral and equatorial ionospheres converged. J. Geophys. Res. Space Phys. 120, 8085–8095. http://dx.doi.org/10.1002/2015JA021555.

Martinis, C., Baumgardner, J., Mendillo, M., Wroten, J., Coster, A.J., Paxton, L.J., 2016. Reply to comment by Kil et al. on "The night when the auroral and equatorial ionospheres converged". J. Geophys. Res. Space Phys. 121, 10608–10613. http://dx.doi.org/10.1002/2016JA022914.

McIlwain, C.E., 1961. Coordinates for mapping the distribution of magnetically trapped particles. J. Geophys. Res. 66, 3681–3691. http://dx.doi.org/10.1029/JZ066i011p03681.

Mendillo, M., Baumgardner, J., Aarons, J., Foster, J., Klobuchar, J., 1987. Coordinated Optical and Radio Studies of Ionospheric Disturbances: Initial Results from Millstone Hill. Ann. Geophys. 5A (6), 543–550.

Mendillo, M., Baumgardner, J., Colerico, M., Nottingham, D., 1997a. Imaging science contributions to equatorial aeronomy: initial results from the MISETA program. J. Atmos. Terr. Phys. 59, 1587–1599.

Mendillo, M., Baumgardner, J., Nottingham, D., Aarons, J., Reinisch, B., Scali, J., Kelley, M.J., 1997b. Investigations of thermospheric-ionospheric dynamics with 6300-Å images from the Arecibo Observatory. J. Geophys. Res. 102, 7331–7343. http://dx.doi.org/10.1029/96JA02786.

Mendillo, M., Baumgardner, J., 1982. Airglow characteristics of equatorial plasma depletions. J. Geophys. Res. 87, 7641–7652. http://dx.doi.org/10.1029/JA087iA09p07641.

Mendillo, M., Tyler, A., 1983. The geometry of depleted plasma regions in the equatorial ionosphere. J. Geophys. Res. 88, 5778–5782. http://dx.doi.org/10.1029/JA088iA07p05778.

Mendillo, M., Baumgardner, J., Pi, X., Sultan, P.J., Tsunoda, R., 1992. Onset conditions for equatorial spread *F*. J. Geophys. Res. 97 (A9), 13865–13876. http://dx.doi.org/10.1029/92JA00647.

Mendillo, M., Zesta, E., Shodhan, S., Sultan, P.J., Doe, R., Sahai, Y., Baumgardner, J., 2005. Observations and modeling of the coupled latitude-altitude patterns of equatorial plasma depletions. J. Geophys. Res. 110, A09303. http://dx.doi.org/10.1029/2005JA011157.

Mendillo, M., Baumgardner, J., Wroten, J., 2016. SAR arcs we have seen: evidence for variability in stable auroral red arcs. J. Geophys. Res. Space Phys. 121, 245–262. http://dx.doi.org/10.1002/2015JA021722.

Miller, C., Swartz, W., Kelley, M., Mendillo, M., Nottingham, D., Scali, J., Reinisch, B., 1997. Electrodynamics of midlatitude spread F, 1. Observations of unstable gravity wave-induced ionospheric electric fields at tropical latitudes. J. Geophys. Res. 102 (A6), 11521–11532.

Moore, J., Weber, E., 1981. OI 6300 and 7774A airglow measurements of equatorial plasma depletions. J. Atmos. Terr. Phys. 43, 851–855. http://dx.doi.org/10.1016/0021-9169(81)90063-5.

Otsuka, Y., Shiokawa, K., Ogawa, T., Wilkinson, P., 2002. Geomagnetic conjugate observations of equatorial airglow depletions. Geophys. Res. Lett. 29, 15. http://dx.doi.org/10.1029/2002GL015347.

Otsuka, Y., Shiokawa, K., Ogawa, T., Wilkinson, P., 2004. Geomagnetic conjugate observations of medium-scale traveling ionospheric disturbances at midlatitude using all-sky airglow imagers. Geophys. Res. Lett. 31, L15803. http://dx.doi.org/10.1029/2004GL020262.

Pimenta, A.A., Kelley, M.C., Sahai, Y., Bittencourt, J.A., Fagundes, P.R., 2008. Thermospheric dark band structures observed in all-sky OI 630 nm emission images over the Brazilian low-latitude sector. J. Geophys. Res. 113, A01307. http://dx.doi.org/10.1029/2007JA012444.

Pavlov, A., 1997. Subauroral red arcs as a conjugate phenomenon: comparison of OV1-10 satellite data with numerical calculations. Ann. Geophys. 15 (8), 984–998. http://dx.doi.org/10.1007/s00585-997-0984.

Reed, E., Blamont, J., 1974. Observations of the conjugate SAR arcs of September 28–30, 1967. J. Geophys. Res. 79, 2269–2555. http://dx.doi.org/10.1029/JA079i016p02524.

Rees, M.H., Roble, R.G., 1975. Observations and theory of the formation of stable auroral red arcs. Rev. Geophys. Space Phys. 13, 201–242.

Rees, M.H., Roble, R.G., 1986. Excitation of O(^{1}D) atoms in aurorae and emissions of the [OI] 6300-Å. Can. J. Phys. 64, 1608–1613.

Richmond, A.D., 1995. Ionospheric electrodynamics using magnetic apex coordinates. J. Geomagn. Geoelectr. 47, 191–212.

Rider, K., Immel, T., Taylor, E., Craig, W., 2015. ICON: where earth's weather meets space weather. IEEE Aerosp. Conf. http://dx.doi.org/10.1109/AERO.2015.7119120.

Roach, F.E., Roach, J.R., 1963. Stable 6300 Å auroral arcs in mid-latitudes. Planet. Space Sci. 11, 523–545.

Schunk, R.W., Nagy, A.F., 2009. Ionospheres: Physics, Plasma Physics and Chemistry. Camb. Univ. Press, Cambridge (UK).

Semeter, J., Mendillo, M., Baumgardner, J., 1999. Multispectral tomographic imaging of the midlatitude aurora. J. Geophys. Res. 104, 24565–24585. http://dx.doi.org/10.1029/1999JA900305.

Semeter, J., Mendillo, M., Baumgardner, J., Holt, J., Hunton, D., Eccles, V., 1996. A study of oxygen 6300Å airglow production through chemical modification of the nighttime ionosphere. J. Geophys. Res. 101 (A9), 19683–19700. http://dx.doi.org/10.1029/96JA01485.

Sharma, A.K., Nade, D.P., Nikte, S.S., Patil, P.T., Ghodpage, R.N., Vhatkar, R.S., Rokade, M.V., Gurubaran, S., 2014. Occurrence of equatorial plasma bubbles over Kolhapur. Adv. Space Res. 54 (3), 435–442.

Shiokawa, K., Otsuka, Y., Tsugawa, T., Ogawa, T., Saito, A., Ohshima, K., Kubota, M., Maruyama, T., Nakamura, T., Yamamoto, M., Wilkinson, P., 2005. Geomagnetic conjugate observation of nighttime medium- scale and large-scale traveling ionospheric disturbances: FRONT3 campaign. J. Geophys. Res. 110, A05303. http://dx.doi.org/10.1029/2004JA010845.

Shiokawa, K., Otsuka, Y., Lynn, K.J., Wilkinson, P., Tsugawa, T., 2015. Airglow-imaging observation of plasma bubble disappearance at geomagnetically conjugate points. Earth Planets Space 67, 43. http://dx.doi.org/10.1186/s40623-015-0202-6.

Slater, D., Smith, L., 1981. Modulation of stable auroral red (SAR) arc occurrence rates. J. Geophys. Res. 86 (A5), 3669–3671. http://dx.doi.org/10.1029/JA086iA05p03669.

Sobral, J., Abdu, M., Pedersen, T., et al., 2009. Ionospheric zonal velocities at conjugate points over Brazil during the COPEX campaign: experimental observations and theoretical validations. J. Geophys. Res. 114 (A4), A04309. http://dx.doi.org/10.1029/2008JA013896.

Solomon, S.C., Abreu, V.J., 1989. The 630 nm dayglow. J. Geophys. Res. 94, 6817–6824. http://dx.doi.org/10.1029/JA094iA06p06817.

Takahashi, H., Wrasse, C.M., Otsuka, Y., Ivo, A., Gomes, V., Paulino, I., Medeiros, A.F., Denardini, C.M., Sant'Anna, N., Shiokawa, K., 2015. Plasma bubble monitoring by TEC map and 630 nm airglow image. J. Atmos. Terr. Phys. 130, 151–158.

Weber, E., Aarons, J., Johnson, A., 1983. Conjugate studies of an isolated irregularity region. J. Geophys. Res. 88 (A4), 3175–3180. http://dx.doi.org/10.1029/JA088iAp03175.

Weber, E., Buchau, J., Eather, R., Mende, S., 1978. North-south aligned equatorial airglow depletions. J. Geophys. Res. 83, 712–716. http://dx.doi.org/10.1029/JA083iA02p00712.